Quantum Electronics **49** (1) 35–42 (2019)

https://doi.org/10.1070/QEL16824

Coherent elastographic tomography via speckle time multiplexing

A. Schwarz*, N. Ozana*, R. Califa, A. Shemer, H. Genish, Z. Zalevsky

Abstract. **A method is suggested for separating photons coming from different depths of tissue while externally stimulating tissue via infra-sonic vibration. The process of tomographic information extraction using the speckle time multiplexing approach is presented. Use is also made of a modulated laser combining a speckle-pattern tracking method for sensing surface tilting changes with an interferometer for sensing surface *z*-axis changes at the same scan time.**

Keywords: *lasers, distributed-feedback, speckle interferometry, scattering, rough surfaces, Fourier optics and signal processing.*

1. Introduction

One of the important parameters for tissue characterisation is the mechanical property of tissue because pathological and physiological characteristics are related to changes in the biomechanics of tissues. Accurate measurements of tissue biomechanical changes make it possible to better understand physiological processes of tissues, as well as diagnose and improve the treatment of various diseases [1, 2].

During the years, several elastography methods were proposed for noninvasive biomechanical detection of tissues elastic properties. Ultrasound elastography (UE) that was first proposed in 1980 uses stimulation of a tissue with acoustic radiation. Using the ultrasonic imaging (UI) technique, the tissue biomechanics is reconstructed according to tissue deformation [3–6]. Later on, based on the magnetic resonance imaging (MRI) technique, magnetic resonance elastography (MRE) was presented [7, 8]. These two methods are limited by the spatial resolving ability of UI and MRI techniques. The resolution of elasticity imaging by UE is of hundreds of micrometres and with MRE is of several millimetres [9–12]. Another elastography method is based on atomic force microscopy (AFM). The elasticity imaging by AFM is of sub-nanometre resolution. AFM elastography has been mainly applied for cells than for tissues due to the limited field of view and the measurement procedure [13, 14]. Elastographic methods based on optical imaging techniques have been developed in order to fills the gap of imaging scales between organ level (UE, MRE) and cell level (AFM). Optical imaging techniques such as multiphoton microscopy [15], confocal Brillouin microscopy [16], laser speckle imaging [17], and optical coherence tomography (OCT) have been recently developed for elastography.

OCT used in optical coherence elastography (OCE) is a growing field. This field of research, which began two decades ago, is today a breakthrough and rapidly developing study compared to its traditional counterparts such as cell mechanics research methods, medical elastography, UE and MRE. Elastography using OCT was first proposed by Schmitt in 1998 [18] and today it is at the forefront of optical elasticity imaging techniques. OCE focuses on the micro-scale assessment of tissue biomechanics in 3D that is hard to achieve with traditional elastographic methods [19]. There is a wide variety of loading methods in OCE techniques such as static/quasi-static or dynamic (continuous wave or pulsed). These loading methods are applied to the tissue either internally or externally [20–22].

The novelties of the presented paper are as follows: (1) ability to detect high-frequency vibrations using a speckle interferometer, (2) ability to detect *z*-axis movement of a subject in addition to the tilt movement, and (3) ability to extract data of the different elastrographic samples using the presented modulation. Unlike other OCE techniques based on OCT methods, the presented method is based on the speckle analysis and a simple laser source. Another advantage of the presented method is that the mechanical deformation is extracted using the trajectory of speckle patterns. Using simple correlation calculations, this trajectory can be extracted, and the mechanical properties of the tissue can be evaluated. For example, compression OCE in a bi-layer sample makes it possible to determine the dependence of speckle displacement on the depth due to a local strain. The strain and displacement approaches are similar to the presented method. However, the novelty of the presented method is that using a simple source with relatively high coherence length, the elastography properties can be extracted by calculating the tilting of the sample via the detected movements of the speckle patterns.

* These authors contributed equally to this work.

A. Schwarz, A. Shemer Faculty of Engineering and the Nanotechnology center, Bar Ilan University, Webb 1 Ramat Gan, 5290002, Israel; Department of Electrical Engineering, Jerusalem College of Engineering, Schreiboim 26 Jerusalem, 9371207, Israel; e-mail: Ariel.Schwarz@biu.ac.il;
N. Ozana, Z. Zalevsky Faculty of Engineering and the Nanotechnology center, Bar Ilan University, Webb 1 Ramat Gan, 5290002, Israel;
e-mail: Nisan.Uzana@biu.ac.il, Zeev.Zalevsky@biu.ac.il;
R. Califa, H. Genish ContinUse Biometrics Ltd., HaBarzel 32b, Tel Aviv 6971048, Israel;
e-mail: Ran.Califa@cu-bx.com, Hadar.Genish@cu-bx.com

Received 4 October 2018; revision received 6 November 2018
Kvantovaya Elektronika **49** (1) 35–42 (2019)
Submitted in English

2. Theoretical background

2.1. Tilting and z-axis detection

The speckle pattern method is based on temporal tracking of a secondary reflected speckle by imaging the speckle through properly defocused optics. The tilting changes of the object surface reflect the movement of the speckle pattern in the xy plane [23–25]. The temporal tilting movement of the object surface is proportional to the change in the spatial position of the speckle pattern:

$$\beta = \frac{4\pi \tan\alpha}{\lambda} \approx \frac{4\pi\alpha}{\lambda}, \quad (1)$$

where β is the change in the speckle pattern, α is the time varying tilting angle of the object illuminated surface, and λ is the illumination wavelength. By calculating the correlation, the relative movement of patterns can be extracted. This relative movement is obtained by allocating the time varying position of the correlation peak.

In order to obtain full surface vibration data, an interferometer is used to detect the temporal changes of the surface in the z axis. The laser source beam splits into two similar paths with only one beam being reflected from the vibrated object. As a result, phase shifts are produced between the two beams caused by a change in the length of one of the paths. These phase shifts create an interference pattern (fringes). The number of wavelengths contained in the path's length difference changes the oscillating frequency of the fringes. Using the laser Doppler vibrometer (LDV) technique the velocity of the object surface vibration in the z axis is measured. The vibration velocity and frequency are extracted from the Doppler shift of the reflected laser beam due to the motion of the surface. The operation of the system is described in Fig. 1.

In order to monitor the z-axis vibrations, we analyse the interference pattern behaviour. The constructive and destructive interference patterns are determined by the length difference ΔL between the two paths, respectively:

$$\Delta L = \pm n\lambda, \quad \Delta L = \pm(n + 1/2)\lambda, \quad (2)$$

where n is the number of illumination wavelengths in ΔL. By analysing the movement in the fringe imaging we can extract the changes in the velocity of the object's path. The frequency of the fringe movement is equal to the frequency of the object movement multiplied by the number of illumination wavelengths λ in the length difference ΔL (the depth of the object movement). For example, for the object movement with amplitude $\Delta L = 1$ mm and frequency of 1–2 Hz (heart beats) at a laser wavelength of 532 nm, the fringe patterns will move at a frequency of 1880–3760 Hz.

This situation of frequency multiplication leads to a problem of camera limited frame rate. In order to solve this problem, use is made of laser modulation, with the laser light pulsating at a frequency of f_1 and the interferometer mirror moving at a frequency f_2 (Fig. 2). In the regular case, the speckle flickers at a frequency of μ_1 due to tilting and the fringe moves at a frequency of μ_2 due to axial movement. In our case, due to the modulation at f_1 and f_2 we obtain the following: the fringe will move at $\mu_2 + f_1 + f_2$ and the speckle will move at $\mu_1 + f_1$. The result is that we actually can use a low sampling rate camera (and thus use many pixels in space and carry out a large field-of-view analysis) since the laser will perform optical down conversion of the spectral distribution to the low band region (because it realises the optical sampling procedure) and the frequency of the mirror f_2 together with the spatial information will allow one to separate between the tilting and the axial movements. Due to the pulsation of the laser we can down convert high temporal frequencies to allow their sampling with a slow rate camera. The high frequencies are folded into the low frequency spectral band sampled by the camera.

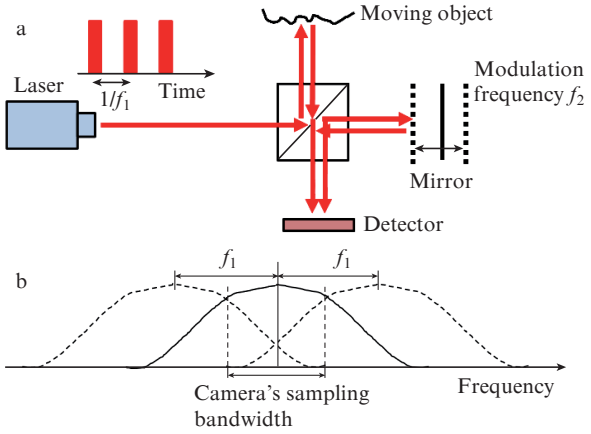

Figure 2. (a) Schematic of the optical system (Michelson or Mach–Zehnder interferometer) and (b) spectral replications with a shift by the pulse repetition rate of the laser.

The modulation frequency was such that the difference between it and the object frequency bandwidth is in the camera limited frame rate:

$$\cos(\lambda f_1 kt)\cos(\lambda f_2 kt) = \frac{\cos(f_1 - f_2)\lambda kt + \cos(f_1 + f_2)\lambda kt}{2}, \quad (3)$$

where k is the wave number. The difference between the two frequencies $(f_1 - f_2)$ can be detected by the slow rate camera

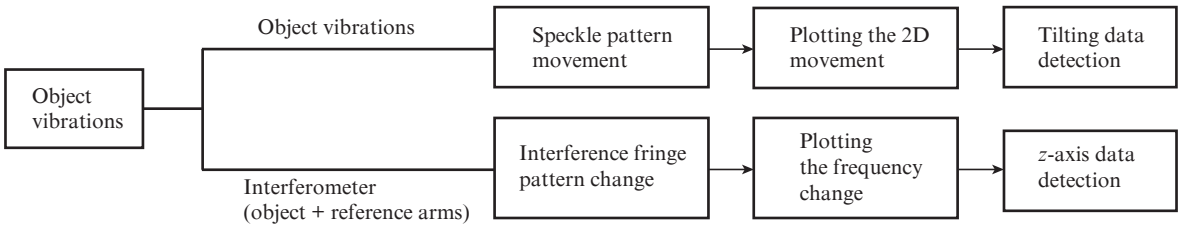

Figure 1. Flow chart of the operation system.

and every change in the system frequency due to the object changes can be detected.

2.2. Elastography

Let us assume that we vibrate a tissue at a frequency of v_1 and that the tissue has two layers. We assume that the photons coming from the inner layer have an electrical field denoted by E_1 and the photons coming from the outer layer have an electrical field denoted by E_2. Since the tissue is soft, the two different layers (in our case there are two layers, but the model can be expanded to a larger number of layers) move asynchronously: Both layers vibrate at the same frequency but there is a time varying shift in their movement profile. This means that photons coming from layer 1 and layer 2 will interfere in the camera but the interference pattern will vary in time with a frequency that is low in comparison to the frequency of the patterns resulting from photons reflected from the same layer. We also assume that the movement amplitude is larger than the size of the scattering points in the tissue. This means that the scattering points move in the tissue otherwise no amplitude movement will be present. Those assumption are needed as we wish to prove that due to the lack of synchronisation and since the integration period of the camera is much larger than $1/v_1$, the electrical fields E_1 and E_2 are incoherent to each other and add up in intensities and not in fields (i.e. they do not interfere with each other). This is a very important assumption because otherwise the two fields will interfere and create a new equivalent field that will generate a new speckle pattern while our aim is to separate the speckle patterns generated by the fields E_1 and E_2.

We assume that the field E_1 generates speckle patterns with an averaged speckle size of d_1 and the field E_2 generates speckles with an average size of d_2. It is simple to design optics in which the light coming from different depths creates speckle patterns with different speckle dimensions. To simplify the mathematics, we will assume that the first and second speckle patterns (coming from the fields E_1 and E_2, respectively) are modelled as follows:

$$s_1(x) = \frac{1}{\sqrt{2\pi d_1^2}} \sum_n \left\{ \exp\left[-\frac{(x - nd_1)^2}{2d_1^2} \right] \exp(2\pi i \varphi_{1n}) \right\},$$
$$s_2(x) = \frac{1}{\sqrt{2\pi d_2^2}} \sum_n \left\{ \exp\left[-\frac{(x - nd_2)^2}{2d_2^2} \right] \exp(2\pi i \varphi_{2n}) \right\}. \tag{4}$$

Now assuming that both patterns move at a frequency of v_1 and amplitude of layer vibrations is $d \gg d_1, d_2$, we obtain:

$$s_1(x - V_1 t) = \frac{1}{\sqrt{2\pi d_1^2}} \sum_n \left\{ \exp\left[-\frac{(x - V_1 t - nd_1)^2}{2d_1^2} \right] \exp(2\pi i \varphi_{1n}) \right\},$$
$$s_2(x - V_1 t) = \frac{1}{\sqrt{2\pi d_2^2}} \times \sum_n \left\{ \exp\left[-\frac{(x - V_1 t - \delta x(t) - nd_2)^2}{2d_2^2} \right] \exp(2\pi i \varphi_{2n}) \right\}, \tag{5}$$

where $V_1 = dv_1$, $\delta x \in [0, d]$.

At the output plane we interfere the two fields' distributions with the reference field which moves at a frequency of v_2 and add them together in the detector:

$$E_{\text{out}}(x,t) = s_1(x - V_1 t) + s_2(x - V_1 t) + r(x - V_2 t). \tag{6}$$

The reference field is a tilted planar wave with an angular frequency of α:

$$r(x - V_2 t) = \exp[2\pi i \alpha (x - V_2 t)], \tag{7}$$

where $V_2 = v_2/\alpha$ is the movement velocity of the reference beam.

The field in the previous expression is captured as intensity in the detector which also performs time integration (according to the integration time of the camera):

$$I_{\text{out}}(x) = \int |E_{\text{out}}(x,t)|^2 \mathrm{d}t = 1 + \int |s_1(x - V_1 t)|^2 \mathrm{d}t + \int |s_2(x - V_1 t)|^2 \mathrm{d}t + \mathrm{Re}\left[\int s_1(x - V_1 t) s_2^*(x - V_1 t) \mathrm{d}t + \int r^*(x - V_2 t)(s_1(x - V_1 t) + s_2(x - V_1 t)) \mathrm{d}t \right]. \tag{8}$$

The integration time is much larger than $1/v_1$ and $1/v_2$ but smaller than $1/(v_1 - v_2)$. Thus, we obtain

$$I_{\text{out}}(x) = 1 + c_1 + c_2 + \mathrm{Re}\left[\int r^*(x - V_2 t)(s_1(x - V_1 t) + s_2(x - V_1 t)) \mathrm{d}t \right], \tag{9}$$

where c_1 and c_2 are space independent constants and the cross correlation expression is zero because the field distributions of the speckle patterns of s_1 and s_2 are not correlated to each other [having different dimensions and asynchronous movement due to the shift $\delta x(t)$]:

$$\int s_1(x - V_1 t) s_2^*(x - V_1 t) \mathrm{d}t = 0. \tag{10}$$

Let us now examine the expressions

$$\mathrm{Re}\left[\int r^*(x - V_2 t) s_1(x - V_1 t) \mathrm{d}t \right],$$
$$\mathrm{Re}\left[\int r^*(x - V_2 t) s_2(x - V_1 t) \mathrm{d}t \right].$$

To simplify them mathematically we will approximate the expression of s_1 and s_2, at least for the case of two adjacent fringes (speckles) to:

$$s_1(x - V_1 t) \approx \cos^2\left[\frac{\pi}{d_1}(x - V_1 t) + \varphi_1 \right] = \frac{1}{2} + \frac{1}{2}\cos\left[\frac{2\pi}{d_1}(x - V_1 t) + \varphi_1 \right],$$
$$s_2(x - V_1 t) \approx \cos^2\left[\frac{\pi}{d_2}(x - V_1 t) + \varphi_2 \right] = \frac{1}{2} + \frac{1}{2}\cos\left[\frac{2\pi}{d_2}(x - V_1 t) + \varphi_2 \right]. \tag{11}$$

Thus, if we assume that our spatial observation point is $x = 0$ or the x coordinate falling on the peak of one of the speckles, then the expressions in question has the form:

$$\begin{aligned}
\mathrm{Re}[r^*(x - V_2t)s_1(x - V_1t)] &\approx \frac{1}{2}\cos(2\pi\alpha V_2t) \\
&+\frac{1}{2}\cos\left(-\frac{2\pi}{d_1}V_1t + \varphi_1\right)\cos(2\pi\alpha V_2t), \\
\mathrm{Re}[r^*(x - V_2t)s_2(x - V_1t)] &\approx \frac{1}{2}\cos(2\pi\alpha V_2t) \\
&+\frac{1}{2}\cos\left(-\frac{2\pi}{d_2}V_1t + \varphi_2\right)\cos(2\pi\alpha V_2t).
\end{aligned} \tag{12}$$

Thus, the final result will be:

$$\begin{aligned}
\mathrm{Re}\left[\int r^*(x - V_2t)s_1(x - V_1t)\,\mathrm{d}t\right] &= \frac{1}{2}\int\cos(2\pi\alpha V_2t)\,\mathrm{d}t \\
&+\frac{1}{2}\int\sin\left(-\frac{2\pi}{d_1}V_1t + \varphi_1\right)\sin(2\pi\alpha V_2t)\,\mathrm{d}t \\
&+\frac{1}{2}\int\cos\left[2\pi t\left(\alpha V_2 - \frac{V_1}{d_1}\right) + \varphi_1\right]\mathrm{d}t, \\
\mathrm{Re}\left[\int r^*(x - V_2t)s_2(x - V_1t)\,\mathrm{d}t\right] &= \frac{1}{2}\int\cos(2\pi\alpha V_2t)\,\mathrm{d}t \\
&+\frac{1}{2}\int\sin\left(-\frac{2\pi}{d_2}V_1t + \varphi_2\right)\sin(2\pi\alpha V_2t)\,\mathrm{d}t \\
&+\frac{1}{2}\int\cos\left[2\pi t\left(\alpha V_2 - \frac{V_1}{d_2}\right) + \varphi_2\right]\mathrm{d}t.
\end{aligned} \tag{13}$$

Since the spatial periodicity α as well as $1/d_1$ are of the same order of magnitude and the time averaging integral resulting from the fact that the camera samples the output intensity at a lower rate causes the first two terms of both expressions to vanish (since they change at temporal a frequency of αV_2 or V_1/d_1). The third term in (13) changes (flickers) at temporal frequencies of

$$v_{F_1} = \alpha V_2 - V_1/d_1, \quad v_{F_2} = \alpha V_2 - V_1/d_2. \tag{14}$$

We can choose our parameters to make these two frequencies low enough so that the sampling rate of the camera will be faster and therefore the quantity inverse to the sampling rate (proportional to the integration time) will be smaller than $1/v_{F_1}$ and $1/v_{F_2}$ and thus the third term in both expressions will not be averaged to zero.

The main advantage of using the optical interference loop in addition to the self-interference expressed as the speckle patterns, is that it adds another parameter V_2, which makes it possible, on the one hand, to average to zero the expression

$$\int s_1(x - V_1t)s_2^*(x - V_1t)\,\mathrm{d}t = 0$$

due to the integration time of the camera and, on the other hand, not to average to zero the expression

$$\int\cos\left[2\pi t\left(\alpha V_1 - \frac{V_1}{d_1}\right) + \varphi_1\right]\mathrm{d}t \quad \text{or} \quad \int\cos\left[2\pi t\left(\alpha V_1 - \frac{V_1}{d_2}\right) + \varphi_2\right]\mathrm{d}t$$

and to allow their detection with the camera. Since each of these two expressions flickers or temporally changes at different frequencies, we can separate them and thus to separate signals s_1 and s_2, i.e. photons coming from different depths of the inspected tissue. One can see from equations (11)–(14) that in comparison to OCT, the depth resolution of the presented approach is based on different temporal flickering frequencies of the speckle pattern. The flickering frequencies differ due to the different speckle size generated by the tissue elastographic properties. According to Eqn (15) the depth resolution is determined by the flickering frequency.

3. Experimental results

3.1. Tilting and *z*-axis detection

In our setup we used the Mach–Zehnder interferometer configuration. The vibration of the surface in the z axis changes the length of one of the Mach–Zender laser paths. These changes are reflected in the interference pattern (fringes) of the two beams joined on a detector and in the camera plane.

The setup includes an illumining laser with a beam splitter in order to obtain an object beam and a reference beam. The reference arm of the interferometer consists of adjustable mirrors that can change the length of the reference arm in order to calibrate the interferometer with two similar arm lengths in accordance with its coherence length. Since the laser beam from the reference arm is incident onto the detector and camera directly, while the laser beam from the object arm experiences reflection from the object, the intensities of these laser beams on the detector and in the camera planes are not the same. For that reason, a filter was placed in the reference arm to equal the two path intensities.

In order to detect only a small area of the speckle pattern and the fringe pattern, the detector had a pinhole with a diameter of 200 μm. The fringe pattern was stabilised by correcting the frequency multiplication caused by the number of wavelengths contained in the object path difference. The correction part of the setup consisted of a feedback circuit from the detector back to the reference arm of the interferometer. The output signal from the detector was passed through an op-amp differentiator amplifier with negative feedback. The output signal from the amplifier was fed to an analogue amplifier driver (powered by a dc power supply) that controls a piezo-actuator attached to a mirror in the reference arm. The controlled mirror movement compensates for the instability of the frequency multiplication caused by the changing number of wavelengths in the path length. The schematic of the setup is shown in Fig. 3

The described configuration makes it possible to simultaneously observe the secondary speckle pattern (in order to obtain tilting information) and the interference fringes (in order to measure the phase shift due to the z-axis displacement). To monitor the tilting vibration, the correlation of each of the sequential speckle images is measured. By analysing the changes in the correlation peak position, the relative tilting movement of the object is extracted.

The results show that the high-frequency object signal is modulated to low frequencies within the camera frame rate window according to the frequency difference (Fig. 4).

3.2. Size of the speckles versus tissue depth

The first experimental validation included verification of the fact that the size of the speckles indeed changes as a function of the depth of the tissue from which the speckles are scat-

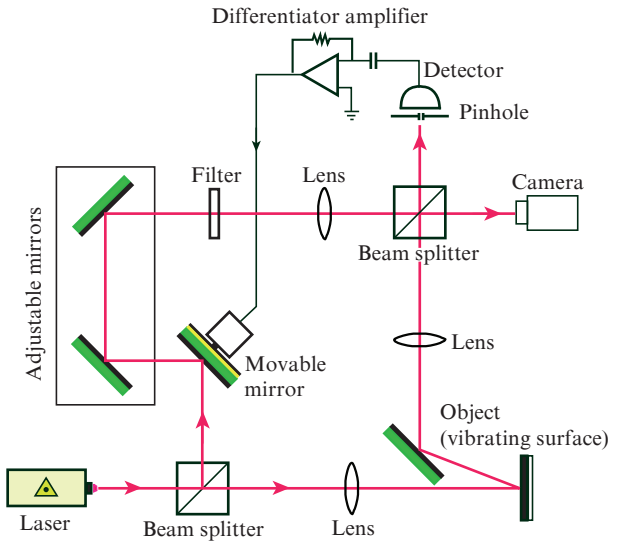

Figure 3. Schematic of the experimental setup for laser pulse modulation.

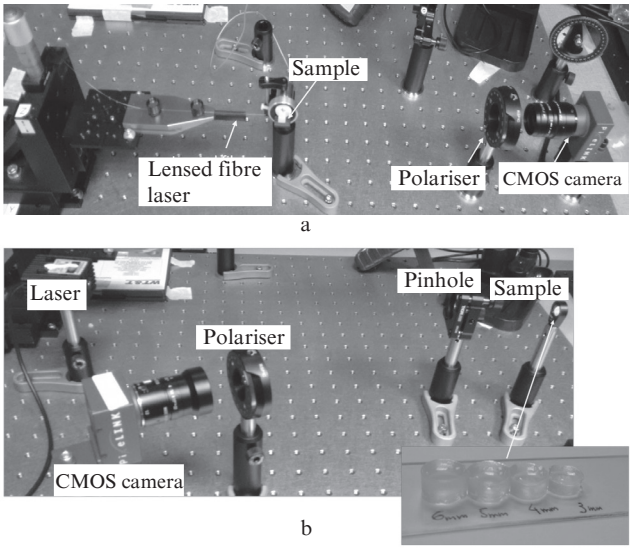

Figure 5. Experimental (a) transmission and (b) reflection setups for testing the size of speckles vs. the thickness of the scattering tissue.

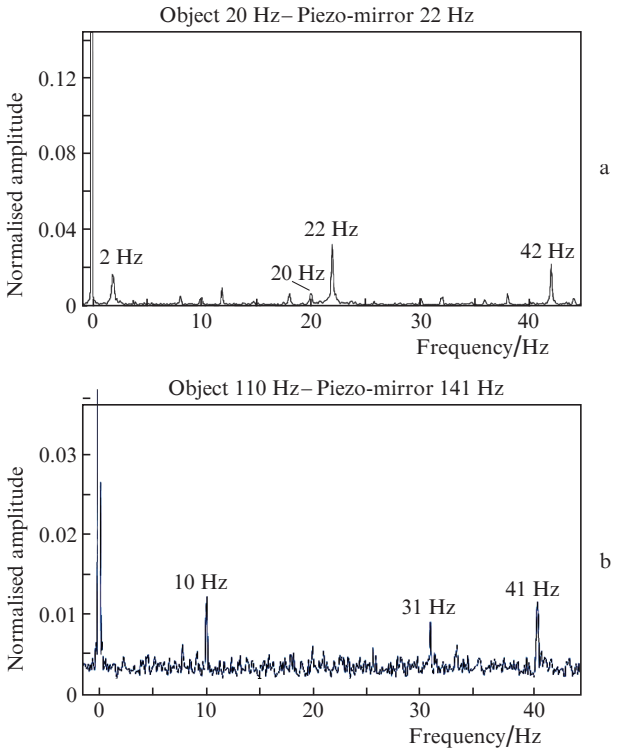

Figure 4. Results of modulation using piezo-mirrors when the high frequency of the object is modulated by the piezo-mirror frequency to low frequencies: (a) the object frequency of 20 Hz, the modulation frequency of 22 Hz, and their difference and addition frequencies; (b) the difference frequency and the cut frequencies (by 100 Hz of the camera) of the object and piezo-mirror.

tered. Two experimental setups were constructed to verify this: the first in transmission (Fig. 5a) and the second in reflection (Fig. 5b). To simulate tissues with different thicknesses proper phantoms were prepared as appearing in the lower right corner of Fig. 5b. The obtained experimental results are seen in Fig. 6. Figure 6a shows the change in the speckle sizes for the transmission experiment and Fig. 6b for reflection. The speckle spot diameters for different layer thicknesses are shown in Fig. 7.

3.3. Coherent elastographic tomography

In order to validate the full proposed concept an experimental setup was assembled (Fig. 8). In this experimental setup we used a different modulation method, instead of a laser pulsation. The vibration of the object (tissues layers) was controlled with a piezo-element at frequency f_1 and position of the interferometer mirror was changed at frequency f_2.

The experimental results are shown in Figs 9 and 10, Fig. 9a showing images of the flickering speckles and Fig. 9b illustrating the spectrum obtained for speckles having different sizes. Figure 9c displays the cut off frequency obtained for speckle having different sizes (corresponding to photons coming from different depths of the inspected tissue). One can see that the cut off frequency of the flickering significantly depends on the thickness of the tissue and thus photons coming from different depths can be separated from each other. It is important to note that proposed concept performs the separation of the photons at the photonic level rather than digitally one (after performing various image processing algorithms). This separation at the photonic level due to temporal modulation and demodulation makes the proposed concept more immune to digital and electronic SNR restrictions that are very dominant in the discussed type of imaging due to a very low SNR involved.

The experimental average results of several experiments with 20 Hz modulations of the speckle flickering system for one and two layers and different concentrations are showed in Fig. 10. The results shown are the standard deviation of several experiments. The following experiments represents the temporal flickering of one layer (0.3% agarose) with respect to a sample with two layers (one with 0.6% of agarose and the second with 0.3% of agarose). Each layer length is equal to 4 mm. Different concentrations of the agarose represent different elastographic layers. One can see that the flickering spectrum pattern changes due to the combination between the layers. The frequency change is proportional to the elastographic value of the layer.

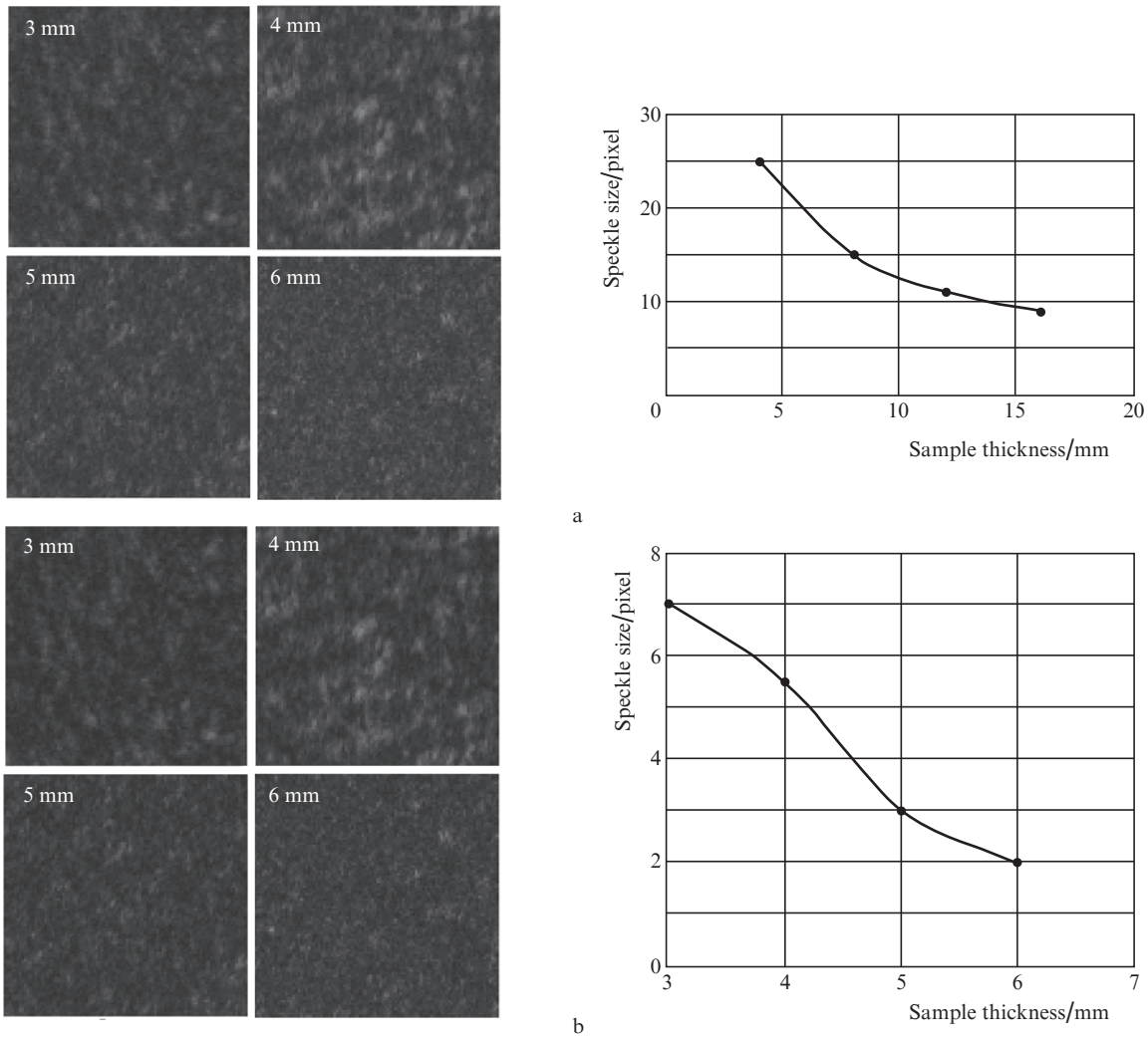

Figure 6. Experimental results for (a) transmission and (b) reflection setups showing the dependence of the speckle size on the thickness of the scattering tissue.

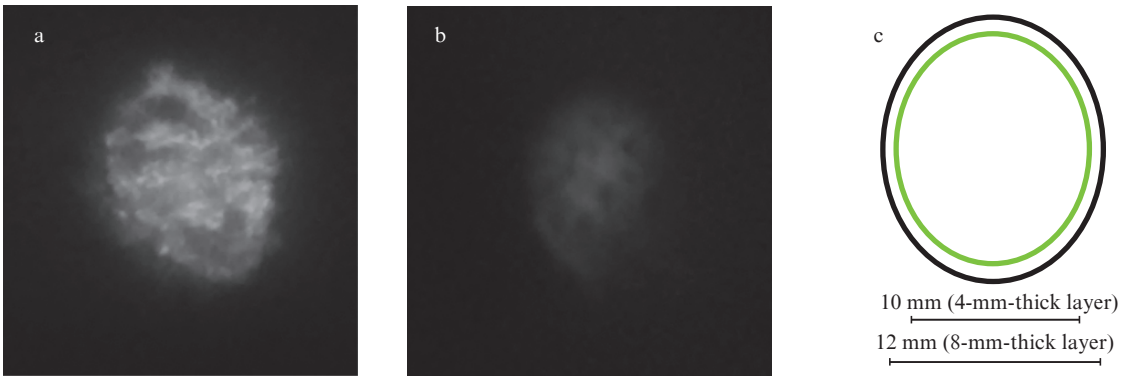

Figure 7. Speckles for (a) 8-mm-thick and (b) 4-mm-thick layers (1 % aragose) and (c) diameters of these speckles.

4. Conclusions

We have shown the possibility of separating data obtained by illuminating different layers of the tissue. We have studied speckle patterns obtained by a Mach–Zehnder interferometer for simultaneous detection of the movement of the whole surface in the z direction and the tilting angle of the surface. Several methods have been proposed to down convert high temporal frequencies to allow their sampling with a slow rate camera. This research shows that different elastographic layers (that are represented by different concentrations of the agarose) change the flickering spectrum pattern, which makes it possible to extractd the elastographic information.

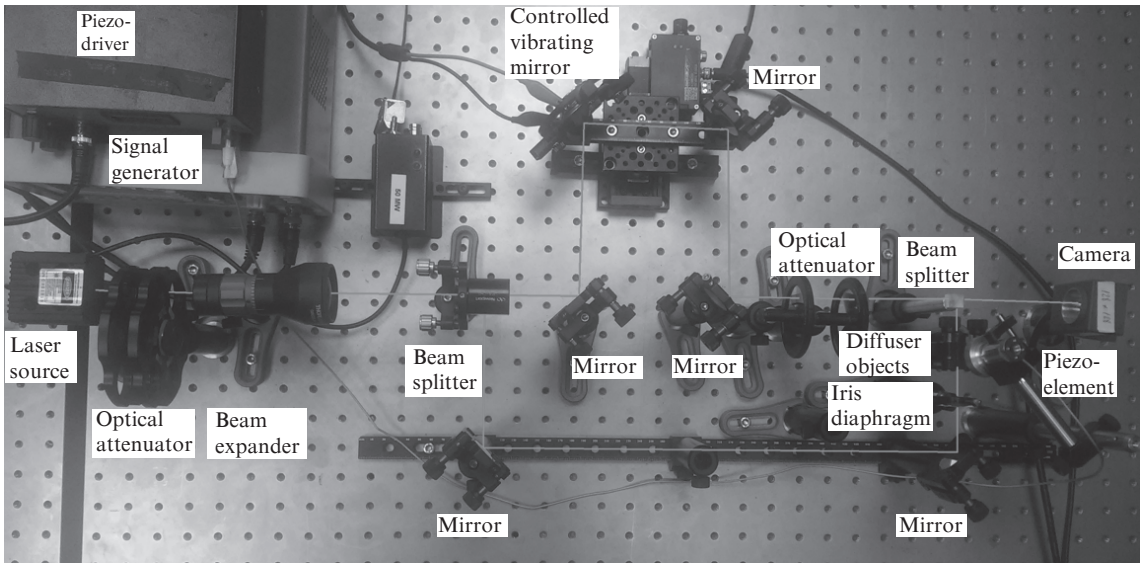

Figure 8. Experimental setup of the coherent elastographic tomography system.

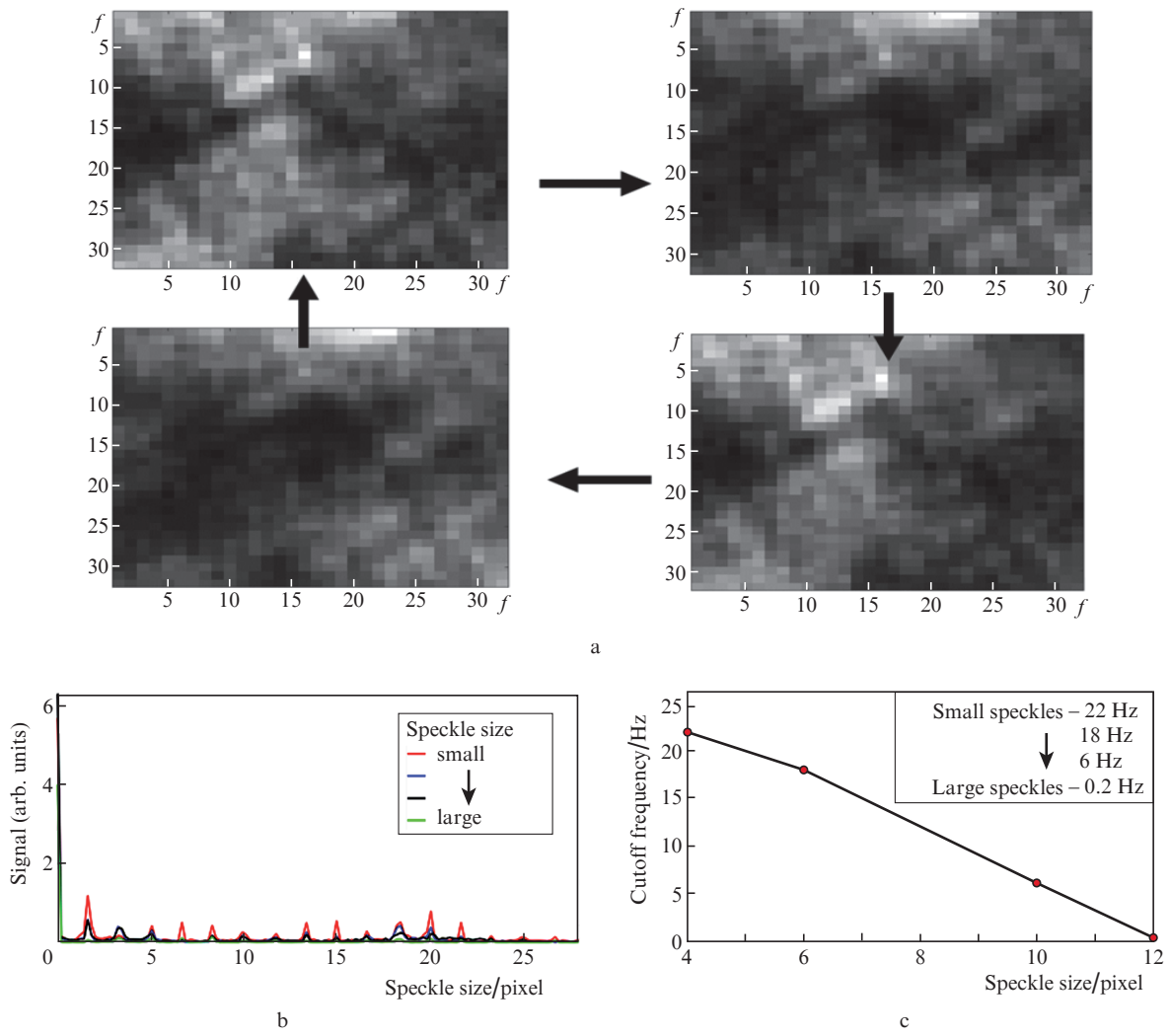

Figure 9. (Colour online) (a) Flickering speckle patterns at different frequencies as functions of the depth of the tissue under study; (b) temporal spectrum of the speckle pattern with different sizes; and (c) cutoff frequencies for different speckle sizes.

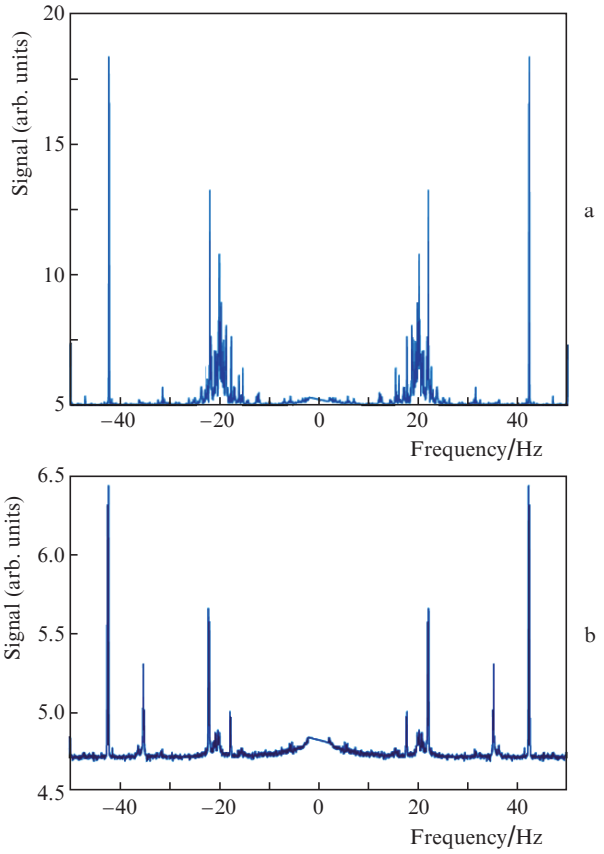

Figure 10. Experimental results of 20-Hz modulations of the speckle flickering system: (a) two layers (0.6%+0.3% concentrations, 4 mm+4 mm thickness) and (b) one layer (0.3% concentration, 4 mm thickness).

References

1. Greenleaf J.F., Fatemi M., Insana M. *Annu. Rev. Biomed. Eng*., **5**, 57 (2003).
2. Yamada H., Evans F.G. *Strength of Biological Materials* (Philadelphia: Lippincott Williams & Wilkins, 1970).
3. Mitrofanova S.I., Belaya E.V., Sapuntsov L.E., Khodorov B.I. *Mech. Compos. Mater.*, **15** (4), 482 (1980).
4. Ophir J., Céspedes I., Ponnekanti H., Yazdi Y., Li X. *Ultrason. Imaging*, **13** (2), 111 (1991).
5. Sarvazyan A.P., Rudenko O.V., Swanson S.D., Fowlkes J.B., Emelianov S.Y. *Ultrasound Med. Biol*., **24** (9), 1419 (1998).
6. Lerner R.M., Parker K.J. *Proc. 7th European Commun. Workshop: Ultrasonic Tissue Characterization and Echographic Imaging*, **7**, 127 (1987).
7. Muthupillai R., Lomas D.J., Rossman P.J., Greenleaf J.F., Manduca A., Ehman R.L. *Science*, **269** (5232), 1854 (1995).
8. Manduca A., Oliphant T.E., Dresner M.A., Mahowald J.L., Kruse S.A., Amromin E., Felmlee J.P., Greenleaf J.F., Ehman R.L. *Med. Image Anal*., **5** (4), 237 (2001).
9. Righetti R., Ophir J., Ktonas P. *Ultrasound Med. Biol*., **28** (1), 101 (2002).
10. Thitaikumar A., Righetti R., Krouskop T.A., Ophir J. *Phys. Med. Biol*., **51**, 5245 (2006).
11. Braun J., Guo J., Lützkendorf R., Stadler J., Papazoglou S., Hirsch S., Sack I., Bernarding J. *NeuroImage*, **90**, 308 (2014).
12. Johnson C.L., McGarry M.D.J., van Houten E.E.W., Weaver J.B., Paulsen K.D., Sutton B.P., Georgiadis J.G. *Magn. Reson. Med*., **70**, 404 (2013).
13. Rotsch C., Radmacher M. *Biophys. J*., **78**, 520 (2000).
14. Kirmizis D., Logothetidis S. *Int. J. Nanomedi.*, **5**, 137 (2010).
15. Liang X., Graf B.W., Boppart S.A. *Cell. Mol. Bioeng*., **4** (2), 231 (2011).
16. Scarcelli G., Yun S.H. *Nature Photon*., **2**, 39 (2008).
17. Jacques S.L., Kirkpatrick S.J. *Opt. Lett*., **23** (11), 879 (1998).
18. Schmitt J. *Opt. Express*, **3** (6), 199 (1998).
19. Wang S., Larin K.V. *J. Biophoton.*, **8** (4), 279 (2015).
20. Liang X., Crecea V., Boppart S.A. *J. Innov. Opt. Health Sci*., **3** (4), 221 (2010).
21. Sun C., Standish B., Yang V.X. *J. Biomed. Opt*., **16** (4), 043001 (2011).
22. Kennedy B.F., Kennedy K.M., Oldenburg A.L., Adie S.G., Boppart S.A., Sampson D.D. *Optical Coherence Tomography*. Ed. by W. Drexler, J.G. Fujimoto (New York: Springer, 2015) p. 1007.
23. Zalevsky Z., Mendlovic D. *Appl. Opt*., **34** (5), 828 (1995).
24. Zalevsky Z., Beiderman Y., Margalit I., Gingold S., Teicher M., Mico V., Garcia J. *Opt. Express*, **17** (24), 21566 (2009).
25. Garcia J., Zalevsky Z., Garcia-Martinez P., Ferreira C., Teicher M., Beiderman Y. *JPCS*, **139**, 012026 (2008).